Binder jet printed WC infiltrated with pre-made melt of WC and Co

Corson L. Cramer[1,*], Trevor G. Aguirre[1], Natalie R. Wieber[1], Richard A. Lowden[2], Artem Trofimov[2], Hsin Wang[2], Jiaqiang Yan[2], M. Parans Paranthaman[3], Amy M. Elliott[1]

[1]*Energy & Transportation Science Division, Energy and Environmental Sciences Directorate, Oak Ridge National Laboratory, Oak Ridge, TN, USA*

[2]*Materials Science and Technology Division, Physical Sciences Directorate, Oak Ridge National Laboratory, Oak Ridge, TN, USA*

[3]*Chemical Sciences Division, Oak Ridge National Laboratory, Oak Ridge, TN, 37831 USA*

*cramercl@ornl.gov

Abstract

WC-Co was made via binder jet additive manufacturing of tungsten carbide followed by melt infiltration with a Co-WC infiltrant. The goal of the study was to achieve fully densified parts in near-net shape with minimal shrinkage while keeping the Co content low. The exact amount of infiltrant was determined in order to fully densify with minimum shrinkage based on the actual volume taken up by WC powder in the preform based on theoretical density, the bounding volume of prints after shrinkage, and the volume from the infiltrant. The eutectic nature of the infiltrant enabled melting at much lower temperature compared to the melting temperature of pure Co. The density, microstructure, grain size, hardness, and fracture toughness were characterized. The shrinkage and net shaping were assessed with light scans. A detailed look at the fracture mechanics was assessed. This approach achieved highly dense WC-Co parts in net-shape with Co vol.% of near 29 (Co wt.% ~19), density of 96.2 % theoretical, hardness of 8.34 GPa, grain size of 7.7 μm,

magnetic saturation of 0.5 T, room temperature thermal conductivity of 125 W/mK, and fracture toughness of 24.7 MPa·$m^{1/2}$.

Keywords: Binder jet additive manufacturing; WC-Co; Eutectic; Infiltration

Introduction

Tungsten carbide-cobalt (WC-Co) is an important material for cutting tools and mining bits, and they have been used in industry since 1923 because of high hardness and fracture toughness, improved wear resistance, and improved strength at high temperatures [1]–[4]. Typically, WC-Co is made with a press and sinter method with composite powders [5], but new methods such as additive manufacturing (AM) have offered more complexity, high throughput, and lower costs.

Some of the emerging manufacturing methods of WC-Co include injection molding, slurry or paste extrusion with direct ink writing or robocasting methods, selective laser melting (SLM) AM, and binder jet AM (BJAM) [6]–[15]. The details of these processes were reviewed more extensively in [13]. The binder jet studies showed how spray-dried, composite powders can be printed and sintered. However, post-processing by hot isostatic pressing (HIP) is needed and the overall shrinkage from processing was as high as 26% linear. BJAM studies on the infiltration of BJAM printed WC and Co showed promise. However, there was large distortion during processing due to the large amount of Co needed for infiltration in order to fill the porosity of the WC preforms, and dissolution of the ceramic preform into the molten material contributed to decreased shape

retention [13], [16]. The infiltration method with current BJAM approach can be improved by engineering the infiltrant and processing.

In the present research, WC preforms were printed with binder jet additive manufacturing and infiltrated with pre-made WC-Co compositions to enable lower temperature processing and redistribution of WC from infiltrant into printed part. No runners nor packing of parts was necessary. The processing and properties of infiltrated parts was investigated.

Materials and Methods

Materials, Processing, and Characterization

The mostly regular-shaped WC powder (-325 mesh from AEE, D_{50} ~ 20 μm), Co ingots, and printing conditions in this study were the same as [17]. Bars of 25 mm width and length with arbitrary thicknesses were printed, as in Figure 1C, so that the height could be cut to size to for testing infiltrant composition. It was easier to adjust specimen size than it was to control the amount of the pre-made infiltrant. Infiltrant was pre-made by melting Co ingot into WC powder in compositions of 50 and 80 wt.% Co as shown in Figure 1A. The primary reason for using the WC-80 wt.% Co as an infiltrant is to allow melting to occur at lower temperature because of the eutectic made in the WC-Co system. A secondary reason for adding WC into the infiltrant was to strategically redistribute WC from the infiltrant into the printed WC preform because the WC in the infiltrant will dissolve in the Co, the Co with dissolved WC will wick into the WC preform,

and the WC will redistribute in the WC preform from reprecipitation of previously dissolved WC during cooling.

After printing, the preforms were debinded and sintered with the same furnace and heating schedule as in [13], and the linear shrinkage value is used from this work. Then, the exact size of the preform and infiltrant were measured in order to make highly dense composite. Infiltrant ingots were sliced into pieces with wire electron discharge machining (EDM) (as shown in Figure 1B) and used for infiltration by placing them under WC prints during heating as shown in Figure 1D. It was hypothesized that the volume of the part after infiltration and shrinkage is equal to the volume taken up by the WC in the green part plus the volume taken up by the infiltrant. Knowing those entities helped calculate the amount of infiltrant relative to the preform to use for infiltration to achieve fully dense composites as in Equation (1).

$$V_{after\ shrinkage} = V_{WC\ in\ green\ part} + V_{Co\ and\ WC\ in\ infiltrant} \quad (1)$$

For this process, the infiltrant amount was calculated by Equation (2), where $m_{Co-20\ wt.\%\ WC}$ is the infiltrant mass amount, $V_{print,\ bounding}$ is the total bounding volume of the part from SolidWorks, $V_{WC\ in\ green\ part}$ is the volume the WC takes up in the printed part and can also be expressed as $(\frac{m_{printed\ WC}}{\rho_{WC}})$. Once the infiltrant and WC print amounts were calculated and ready for processing, the samples were setup as in Figure 1C. The furnace was heated to 1400°C at 10°C/min with a 10 min hold in Ar/4%H_2 atmosphere in an alumina tube furnace. Several attempts to infiltrate the WC preforms with Co-50 wt.% WC were unsuccessful. The Co-50 wt.% WC did not fully penetrate the WC preform, most likely due to large amount of WC

particles in the infiltrant being filtered by the porous surface of the WC preform. In these experiments, WC was left on the outside of the preform infiltrated with Co-50 wt.% WC. Because of this result, the focus of the characterization is on the infiltration of the Co-20 wt.% WC into WC preforms. Based on the green density, preliminary shrinkage results, and pre-made infiltrant compositions, it is hypothesized using Equation 1 that near net shaping of WC-Co is achievable with high density with volume fraction of Co near 30%. Figure 2A shows the experimental setup for the preform and infiltrant processing.

$$m_{Co-20\ wt.\%\ WC} = \frac{5\ \rho_{WC}\rho_{Co}\left(\frac{V_{print,\ bounding}}{(1.15)^3} - V_{WC\ in\ green\ part}\right)}{4\rho_{WC} + \rho_{Co}} \quad (2)$$

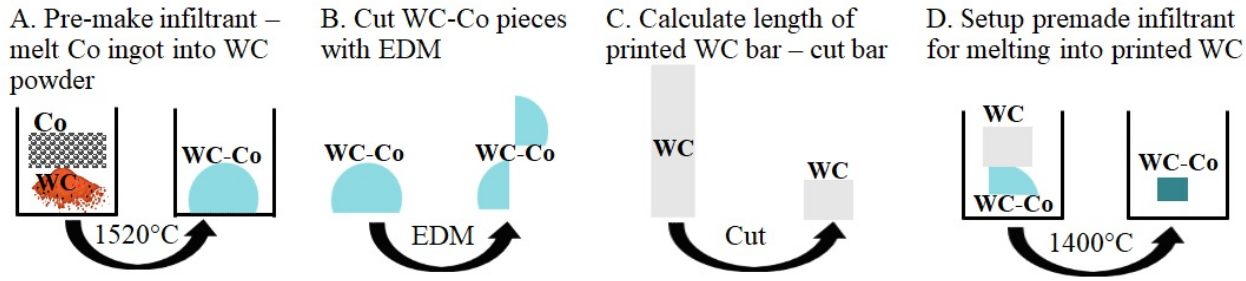

Figure 1: Schematic of the processing sequence.

Material Characterization

Material characterization was the same as in [13]. Dimensional data was collected using a Faro Red Laser Scanner and Geomagic Control 2015. Scans of green and infiltrated parts were aligned in SolidWorks by aligning the center of mass of each scan to assess deviation and shrinkage during processing. Magnetic properties of the printed sample were measured using a Quantum Design

magnetic property measurement system (MPMS) similar to [18], [19]. Thermal conductivity (κ) was indirectly measured by obtaining thermal diffusivity (α) from the laser flash method (Netzsch LFA 457) following ASTM 14611-13 and specific heat (C_p) from differential scanning calorimeter (DSC) on a Netzsch Pegsus 404 system following ASTM 1269-11. Using room temperature density (ρ), thermal conductivity values from room temperature to 800ºC are calculated by the following equation:

$$\kappa = \alpha \rho C_p \tag{3}$$

Mechanical Testing

Fracture toughness of the composites in this study were assessed using the Single Edge Notch Beam Technique [20]. Tests were performed in 4-point bending using a custom 4-point bend testing device with an Instron Model 8501. Notched samples were loaded at 1 mm per minute until sample rupture. Specimen sample sizes were 4 × 4 × 22 mm. Vickers hardness was measured using a LECO LM 110AT apparatus with an applied load of 0.5 kgf and an Instron, Wilson-Wolpert 2100B apparatus with an applied load of 10 kgf, both holding the load for 15 seconds.

Results and Discussion

Figure 2 shows macro images of the experimental setup, processed sample as oriented in the furnace, and the processed sample rotated 90 degrees to show the underside. The setup with the WC resting on top of the infiltrant is similar to [13] and samples did not use runners nor alumina

packing. Even without the use of runners and alumina packing, the samples were near-net shaped. Features such as the number "4" in the corner and some rounded edges were retained during processing, and the infiltrant wicked into the entire sample. Table 1 shows the density of the composites made, which is highly dense for this material. The processing and infiltration of the pre-made Co infiltration was successful by using the eutectic point similar to [21]–[23].

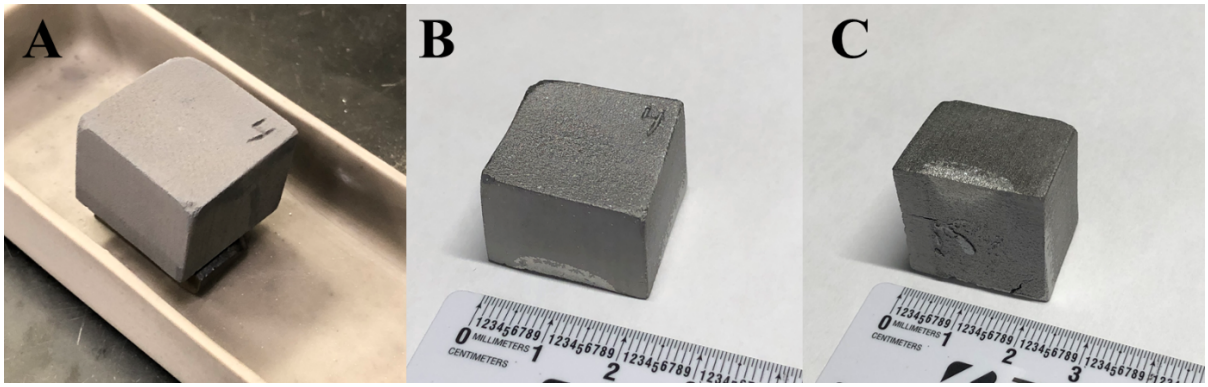

Figure 2: Macro images of A) the experimental setup, B) the infiltrated part orientated as in the furnace, and C) the infiltrated part rotated 90 degrees from the processing orientation.

Table 1: Properties of the WC-Co part.

Co amount (vol.%, wt.%)	Density (g/cc, %TD)	Grain size (μm)	Hardness (GPa) 0.5 kgf, 10 kgf	Fracture toughness (MPa · $m^{1/2}$)
29.1 ± 0.4, 18.9 ± 0.4	13.1 ± 0.3, 96.2 ± 0.3	7.7 ± 1.7	8.24 ± 1.27, 8.34 ± 0.2	24.7 ± 1.5

Figure 3 shows XRD data of samples infiltrated with Co-20 wt.% WC. There are peaks for only WC and Co, indicating minimal ternary phase formed. This is important for WC-Co composites because the ternary phase is more brittle than WC [24], [25]. There were two phases of Co, face centered cubic (FCC) Co and hexagonal close packed (HCP) Co. There was small amount of

HCP Co in the composites as indicated with XRD, so it is likely that the Co had some dissolved species, either C or W, in it to stabilize two different phases of Co.

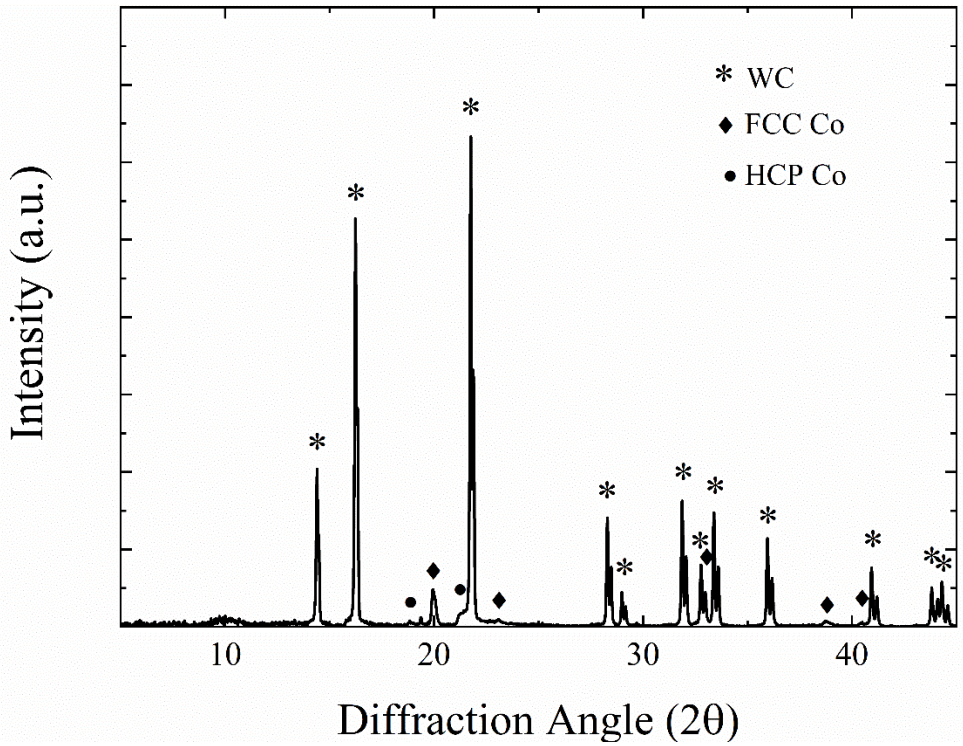

Figure 3: XRD scan of WC prints infiltrated with Co-20 wt.% WC.

Figure 4 shows light scan overlays in SolidWorks of the center of mass of the green and infiltrated parts. The green part is shown in transparent, light gray. The WC sample infiltrated with the Co-20 wt.% WC is represented with the solid, darker gray shade. Clearly, there is some shrinkage and distortion from the process, which usually occurs from liquid phase sintering and solidification of the Co during cooling. It is almost impossible to know which one dominates the shrinkage without *in-situ* monitoring. Nonetheless, the infiltrated sample shows approximately 14% linear shrinkage, which is currently better than all methods of additive manufacturing of

WC-Co with similar compositions. The drawback in the current research is that the volume fraction of Co is still higher compared to the other additive manufacturing approaches for use in cutting tools. This was hypothesized, but it is an implication of low green densities in BJAM. Higher density preforms may help this process.

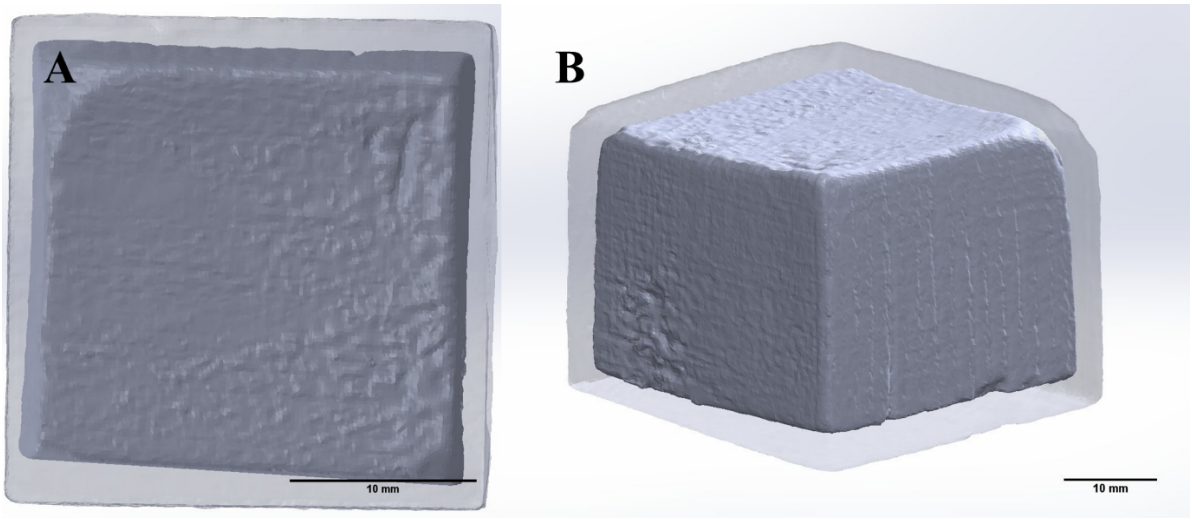

Figure 4: 3D scan overlay and cross sections of green part(transparent gray) versus infiltrated part (solid gray).

Figure 5 shows optical and SEM images of the microstructure of the WC-Co composites. The density was measured by geometric and Archimedes methods using the theoretical density of WC-30 vol.% Co. The density of these composites was measured as 96.2 %TD. 30 vol.% Co was calculated from Equation (2) and verified in ImageJ. The optical image shows some pores between 20-40 micron. These are most likely remnants from the melt infiltration process and trapped air. This conclusion is drawn from the round shaped pores. It is also possible that the pores are from flaws in the printing process. However, this can only be confirmed by CT

scanning of the green parts. The SEM image shows some smaller pores and cracks but mostly the microstructure consisted of contiguous WC grains with 7.7 micrometer average grain size.

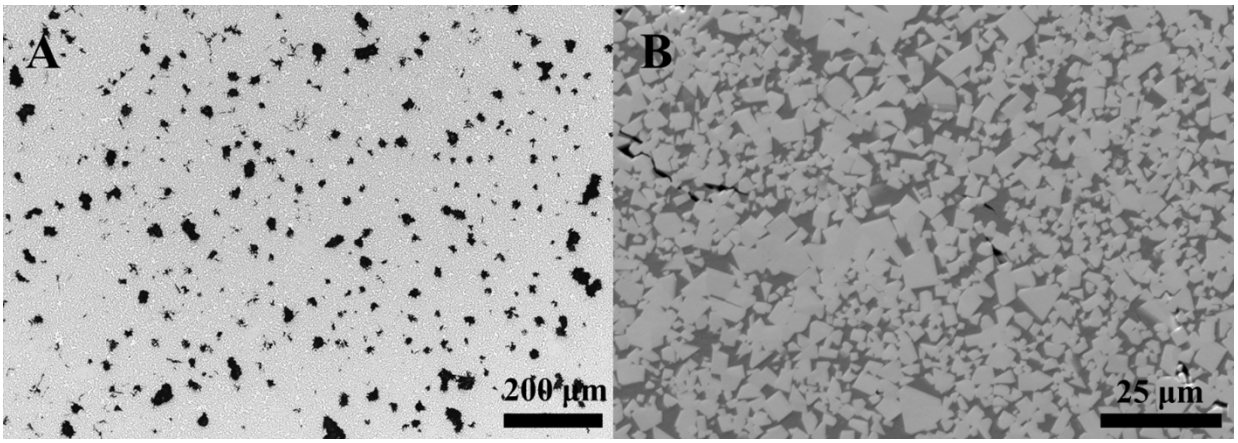

Figure 5: A) Optical and B) SEM images of the microstructure. There are some pores and a mostly contiguous network of WC grains.

Figure 6 shows a macro image of the fractured specimen, SEM of the fracture surface, and SEM of a typical Vickers indent performed with 0.5 and 10 kgf. Figure 6A shows the fractured sample, and there is evidence of brittle and ductile fracture because of the angled cleave compared to similar material composition and grain size [26]. The fracture toughness was slightly higher than conventionally-made WC-Co with similar Co content ~30 vol.% but slightly smaller grain sizes ~1-2 micron with values near 25 $MPa \cdot m^{1/2}$ [27], [28]. Figure 6B shows a typical fracture surface of the WC-Co beams from the single edge notch beams of this study. From this it is observed that small spherical pores are present after the infiltration process. Furthermore Figure 6B shows transgranular fracture of the WC grains as well as some grain pull out.

Figure 6C shows the geometry of a typical Vickers indent with a load of 0.5 kgf. No cracks protrude from the idents, which is indicative of large amounts of Co because it provides some ductility in the composite. Figure 6D shows the geometry of a typical Vickers indent with a load of 10 kgf. There is some spalling but still no protruding cracks, and the spalling can affect the measurements as in [29]. The two hardness values as shown in Table 1 are very similar, and usually lower loads result in lower hardness values [30], which was not observed here. The Vickers hardness values done with the higher load resulted in less deviation from the average values. The hardness of conventionally-made WC-Co with similar Co content and grain size, ~3-8 micron, is roughly ~9.3 GPa [31]–[33], which is slightly higher than the current research. The higher hardness values in the literature may be from the smaller WC grains.

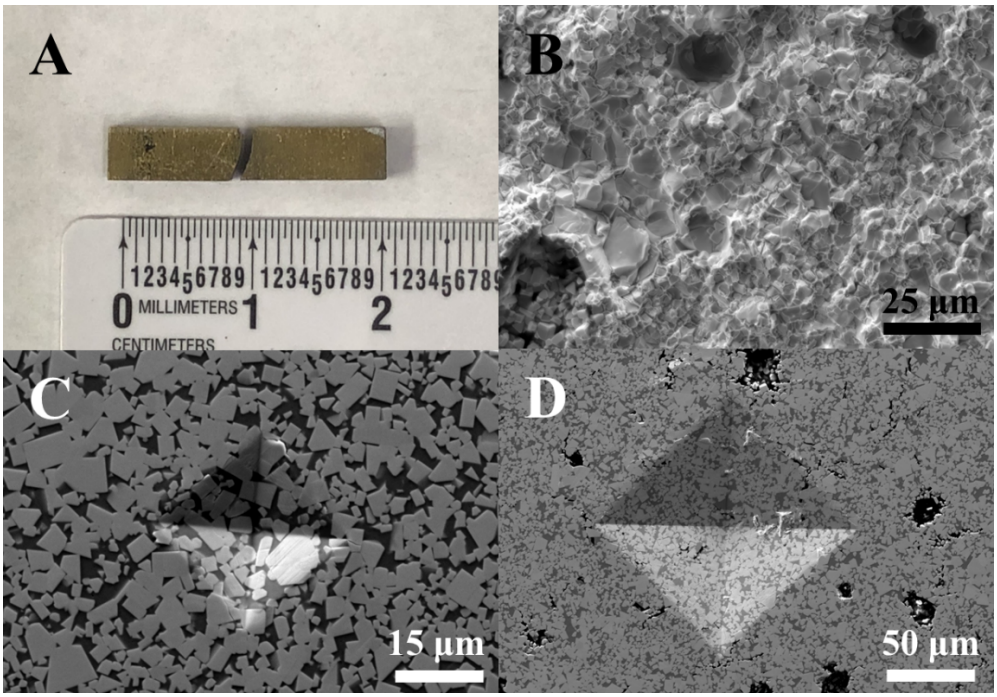

Figure 6: A) Macro image a tested and fractured specimen. B) SEM of the fracture surface. C) SEM of a typical microhardness indent with 0.5 kgf. D) SEM of a typical microhardness indent with 10 kgf.

Figure 7 shows property data of the magnetic saturation and the thermal conductivity. Figure 7A shows the saturation magnetization (Ms) value of the BJAM WC-Co sample measured at 20°C using a SQUID magnetometer. The saturation induction is about 0.5 T. This is similar to values seen in [34] of 0.55 T, where the value in the current research is lower because of grain size differences and residual porosity. Figure 7B is the specific heat values over the same temperature range where the raw data is shown as well as a linear fit for use in the thermal conductivity calculation. Figure 7C is the thermal diffusivity vs. temperature plot of the WC-Co. The room temperature value of 40 mm^2/s decreased to 16 mm^2/s at 800 ºC. Figure 7D is the calculated thermal conductivity of the WC-Co using equation (3) and density of 13.1 g/cm^3. Room temperature thermal conductivity is similar to the literature values of comparable materials [35], [36]. The decrease from 125 W/mK to 60 W/mK is from lattice thermal conductivity due to phonon scattering, which is most likely dominating the transport properties. At higher temperatures, scattering of shorter mean-free-path phonons with grain boundaries, pores and other defects further decreased thermal conductivity.

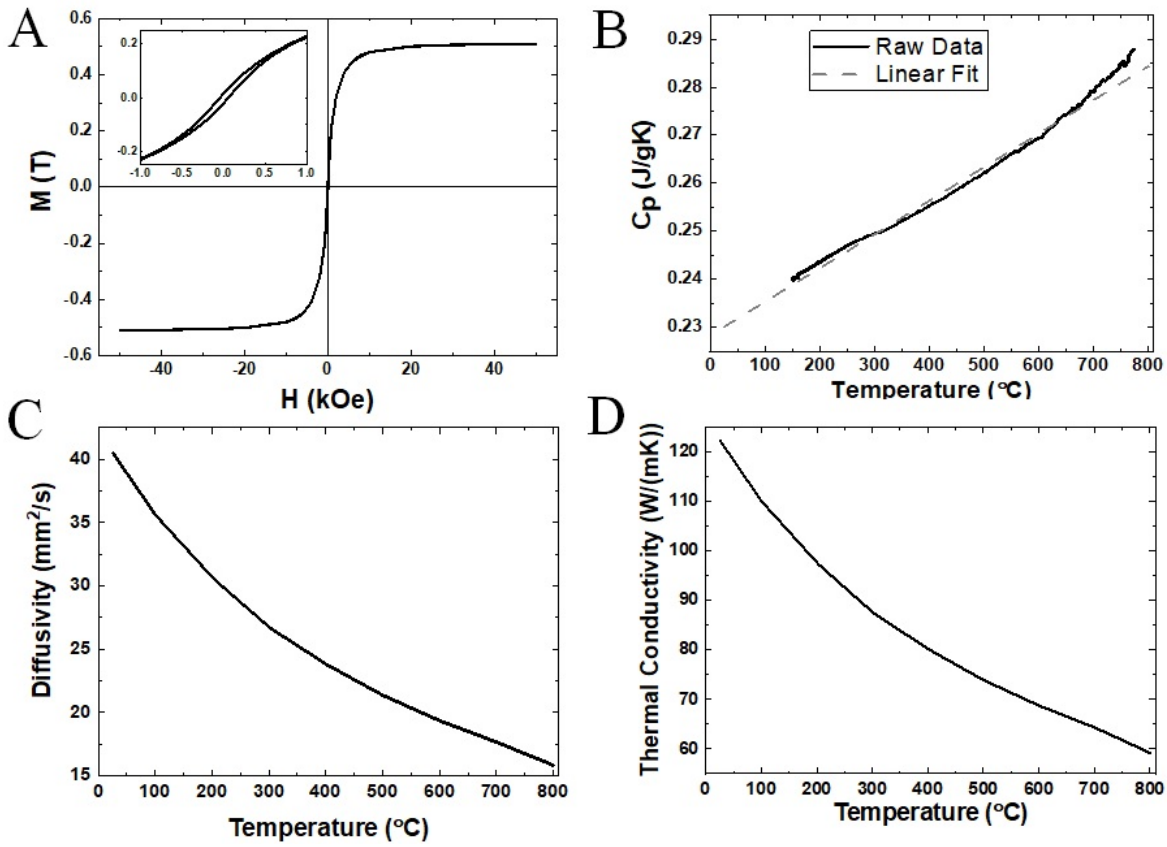

Figure 7: Magnetic saturation at room temperature (A), heat capacity vs. temperature (B), thermal diffusivity vs. temperature (C), and calculated thermal conductivity vs. temperature (D).

Using Equation (2) to accurately predict part volume after shrinkage is demonstrated by this research, and a pseudo-binary phase diagram helps explain the compositions of the pre-made infiltrant and the final consolidated composites. Shown in Figure 8, the starting infiltrant composition provides enough liquid to allow full infiltration to produce WC-Co composites with 19 wt.% Co (29 vol.% Co) by lowering the overall melting temperature, and thus processing temperature. This also allows the processing to occur at much lower temperatures compared to the melting temperature of Co and the temperatures used in liquid-phase sintering [14], [15]. Though lower mass fractions of Cobalt are favorable, our approach provides a low temperature processing route that produces WC-Co composites that have Co composition close to what is

typically used in in WC-Co cutting tools (8-15 wt.% Co [37]). The material made in the current research is ideal for applications needing higher fracture toughness while retaining some hardness and wear properties.

Since the necessary amount of Co is dependent on the starting green density of the WC preform, it is evident that higher WC green densities are necessary to reach lower volume fractions of Co with this method. A preform with high density that has not yet reached closed porosity, roughly 80-90 %TD, is ideal to test infiltration of WC and reach low Co vol.%. Also, if *in-situ* monitoring could be performed during the infiltration, the most dominant shrinkage mechanism, either Co solidification or liquid phase sintering, could be identified. To get *in-situ* monitoring through WC means that neutrons would have to be used. High-speed camera would be a good start to see the process *in situ*.

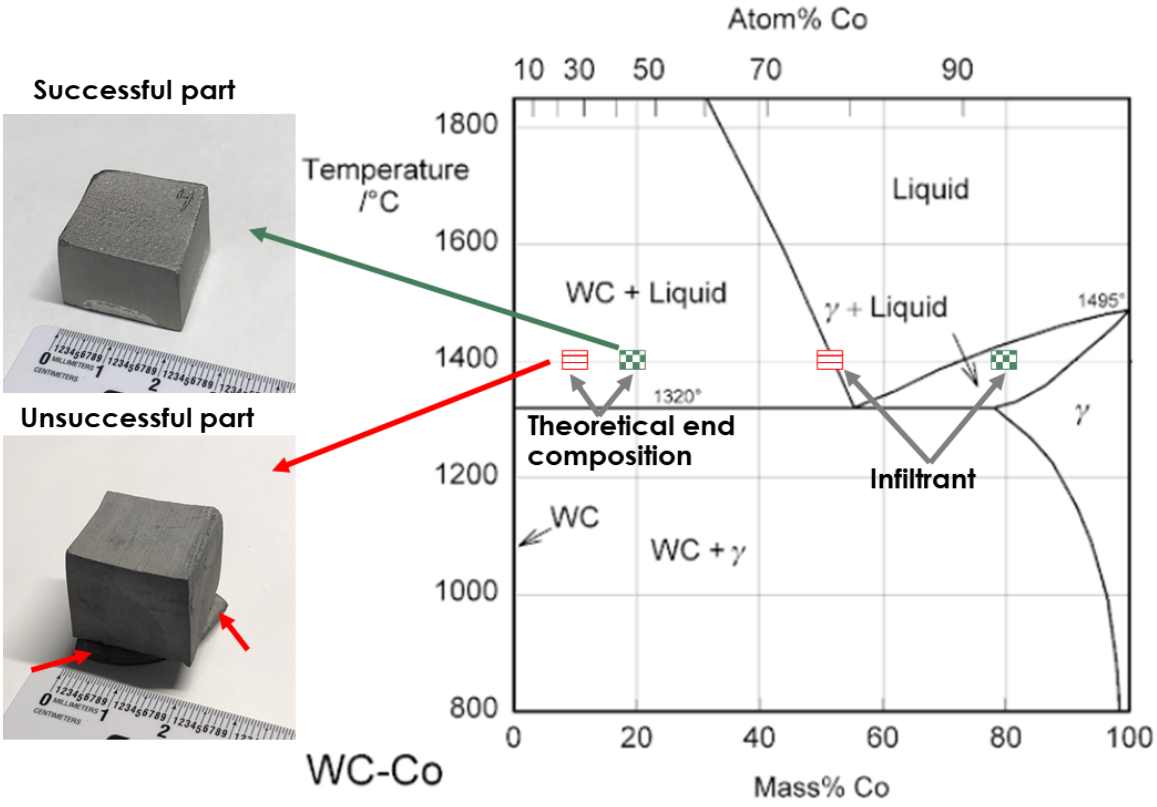

Figure 8: Section of the phase diagram for WC-Co [38]. This system is represented with a pseudo-binary system, so it is assumed that the W and C content are the same throughout the varying amount of Co. The smaller red arrows on the bottom sample show the remaining WC that was filtered out when using infiltration of 50 wt.% WC.

Conclusions

The novel approach presented in this study helped solve the issues of large pits and missing parts of the 3D printed WC as observed in previous work. The processing was enabled by using the WC-20wt% eutectic composition. WC-Co preforms were successfully shaped with minimal distortion and shrinkage by infiltration with a WC-Co infiltrant that has lower melting point compared to pure Co. Due to low green densities of the WC preform, the amount of Co needed for cutting tool applications (8-15wt%) is not reached. Though lower mass fractions of Cobalt are favorable, our approach provides a low temperature processing route for producing WC-Co composites. Shape retention was very high with linear shrinkage of only 14%. Some remaining porosity (~4%) was present after infiltration because shrinkage could not be precisely calculated. However, despite these limitations, 3D printed WC-Co show comparable hardness and fracture toughness to traditionally manufactured WC-Co. Also, the magnetic saturation is similar to WC-Co of similar Co content and grain size. The thermal conductivity is calculated and reported as a function of temperature using heat capacity, thermal diffusivity, and mass density. Overall, this process provides a low-temperature processing route for hard, fracture resistant, and net-shaped WC-Co parts.

Acknowledgments

Corson L. Cramer would like to thank Olivia Shafer for help formatting and editing. This material is based upon work supported by the U.S. Department of Energy, Office of Energy Efficiency and Renewable Energy, Office of Advanced Manufacturing and Propulsion Materials program under the Vehicle Technology Office, under contract number DE-AC05-00OR22725. The magnetic measurement was supported by the Critical Materials Institute, an Energy Innovation Hub funded by the U.S. Department of Energy, Office of Energy Efficiency and Renewable Energy, Advanced Manufacturing Office.

References

[1] B. G. Compton and F. W. Zok, "Impact resistance of TiC-based cermets," *Int. J. Impact Eng.*, vol. 62, pp. 75–87, Dec. 2013.

[2] J. Gurland and T. J. Norton, "Role of binder phase in cemented tungsten carbide-cobalt alloys," *Metals (Basel).*, vol. 194, no. 10, pp. 1051–56, 1952.

[3] R. G. Cornwall and R. M. German, "WC-Co enjoys proud history and bright future," *Met. Powder Rep.*, vol. 53, no. 2, pp. 32–36, Feb. 1998.

[4] P. Ettmayer, "HARDMETALS AND CERMETS," *Annu. Rev. Maler. Sci*, vol. 19, pp. 145–54, 1989.

[5] W. Su, Y. Sun, H. Wang, X. Zhang, and J. Ruan, "Preparation and sintering of WC–Co composite powders for coarse grained WC–8Co hardmetals," *Int. J. Refract. Met. Hard Mater.*, vol. 45, pp. 80–85, Jul. 2014.

[6] Z. Baojun, Q. Xuanhui, and T. Ying, "Powder injection molding of WC–8%Co tungsten

cemented carbide," *Int. J. Refract. Met. Hard Mater.*, vol. 20, no. 5–6, pp. 389–394, Dec. 2002.

[7] U. Scheithauer, "Droplet-Based Additive Manufacturing of Hard Metal Components by Thermoplastic 3D Printing (T3DP)," *doi.org*, no. 01.

[8] B. D. Kernan, E. M. Sachs, M. A. Oliveira, and M. J. Cima, "Three-dimensional printing of tungsten carbide–10wt% cobalt using a cobalt oxide precursor," *Int. J. Refract. Met. Hard Mater.*, vol. 25, no. 1, pp. 82–94, Jan. 2007.

[9] R. S. Khmyrov, V. A. Safronov, and A. V. Gusarov, "Obtaining Crack-free WC-Co Alloys by Selective Laser Melting," *Phys. Procedia*, vol. 83, pp. 874–881, Jan. 2016.

[10] X. C. Wang, T. Laoui, J. Bonse, J. P. Kruth, B. Lauwers, and L. Froyen, "Direct Selective Laser Sintering of Hard Metal Powders: Experimental Study and Simulation," *Int. J. Adv. Manuf. Technol.*, vol. 19, no. 5, pp. 351–357, Mar. 2002.

[11] H. Kyogoku, T. Uemori, A. Ikuta, K. Yoshikawa, and H. Ohmori, "Direct Selective Laser Sintering of WC-Co Cemented Carbide by Premixing of Additives," in *ASME/ISCIE 2012 International Symposium on Flexible Automation*, 2012, p. 465.

[12] R. S. Khmyrov, V. A. Safronov, and A. V. Gusarov, "Synthesis of Nanostructured WC-Co Hardmetal by Selective Laser Melting," *Procedia IUTAM*, vol. 23, pp. 114–119, Jan. 2017.

[13] C. L. Cramer, P. Nandwana, R. A. Lowden, and A. M. Elliott, "Infiltration studies of additive manufacture of WC with Co using binder jetting and pressureless melt method," *Addit. Manuf.*, Apr. 2019.

[14] R. K. Enneti, K. C. Prough, T. A. Wolfe, A. Klein, N. Studley, and J. L. Trasorras, "Sintering of WC-12%Co processed by binder jet 3D printing (BJ3DP) technology," *Int.*

J. Refract. Met. Hard Mater., Oct. 2017.

[15] R. K. Enneti and K. C. Prough, "Wear properties of sintered WC-12%Co processed via Binder Jet 3D Printing (BJ3DP)," *Int. J. Refract. Met. Hard Mater.*, vol. 78, pp. 228–232, Jan. 2019.

[16] J. M. Arnold, C. L. Cramer, A. M. Elliott, P. Nandwana, and S. S. Babu, "Microstructure evolution during near-net-shape fabrication of NixAly-TiC cermets through binder jet additive manufacturing and pressureless melt infiltration," *Int. J. Refract. Met. Hard Mater.*, vol. 84, p. 104985, Nov. 2019.

[17] C. L. Cramer, N. R. Wieber, T. G. Aguirre, R. A. Lowden, and A. M. Elliott, "Shape retention and infiltration height in complex WC-Co parts made via binder jet of WC with subsequent Co melt infiltration," *Addit. Manuf.*, vol. 29, p. 100828, Oct. 2019.

[18] M. P. Paranthaman *et al.*, "Binder Jetting: A Novel NdFeB Bonded Magnet Fabrication Process," *JOM*, vol. 68, no. 7, pp. 1978–1982, Jul. 2016.

[19] C.L. Cramer, P. Nandwana, J. Yan, S.F. Evans, A.M. Elliott, C. Chinnasamy, and M. P. Paranthaman, "Binder Jet Additive Manufacturing Method to Fabricate Near Net Shape Crack-free Highly Dense Fe-6.5 wt.% Si Soft Magnets," *Helyion*, vol. Under Review, 2019.

[20] G. M. L.A. Simpson, T.R. Hsu, "The Application of the Single-Edge Notched Beam to Fracture Toughness Testing of Ceramics," *J. Test. Eval.*, vol. 2, no. 6, p. 503, 1974.

[21] M. Caccia *et al.*, "Ceramic–metal composites for heat exchangers in concentrated solar power plants," *Nature*, vol. 562, no. 7727, pp. 406–409, Oct. 2018.

[22] Y. Zhao, Y. Wang, Y. Zhou, and P. Shen, "Reactive wetting and infiltration of polycrystalline WC by molten Zr2Cu alloy," *Scr. Mater.*, vol. 64, no. 3, pp. 229–232, Feb.

2011.

[23] M. B. Dickerson, P. J. Wurm, J. R. Schorr, W. P. Hoffman, P. G. Wapner, and K. H. Sandhage, “Near net-shape, ultra-high melting, recession-resistant ZrC/W-based rocket nozzle liners via the displacive compensation of porosity (DCP) method,” *J. Mater. Sci.*, vol. 39, no. 19, pp. 6005–6015, Oct. 2004.

[24] D. Stewart, P. Shipway, D. M.-S. and Coatings, and undefined 1998, “Influence of heat treatment on the abrasive wear behaviour of HVOF sprayed WC–Co coatings,” *Elsevier*.

[25] “Tribology of thermal sprayed WC–Co coatings,” *Int. J. Refract. Met. Hard Mater.*, vol. 28, no. 1, pp. 82–94, Jan. 2010.

[26] S. Okamoto, Y. Nakazono, K. Otsuka, Y. Shimoitani, and J. Takada, “Mechanical properties of WC/Co cemented carbide with larger WC grain size,” *Mater. Charact.*, vol. 55, no. 4–5, pp. 281–287, Nov. 2005.

[27] K. S. Ravichandran, “Fracture toughness of two phase WC-Co cermets,” *Acta Metall. Mater.*, vol. 42, no. 1, pp. 143–150, Jan. 1994.

[28] J. L. Chermant and F. Osterstock, “Fracture toughness and fracture of WC-Co composites,” *J. Mater. Sci.*, vol. 11, no. 10, pp. 1939–1951, Oct. 1976.

[29] T. G. Aguirre, C. L. Cramer, V. P. Torres, T. J. Hammann, T. B. Holland, and K. Ma, “Effects of the addition of boron nitride nanoplate on the fracture toughness, flexural strength, and Weibull Distribution of hydroxyapatite composites prepared by spark plasma sintering,” *J. Mech. Behav. Biomed. Mater.*, vol. 93, pp. 105–117, May 2019.

[30] E. Broitman, “Indentation Hardness Measurements at Macro-, Micro-, and Nanoscale: A Critical Overview,” *Tribol. Lett.*, vol. 65, no. 1, p. 23, Mar. 2017.

[31] Y. . Milman, S. Luyckx, and I. Northrop, “Influence of temperature, grain size and cobalt

content on the hardness of WC–Co alloys," *Int. J. Refract. Met. Hard Mater.*, vol. 17, no. 1–3, pp. 39–44, May 1999.

[32] H. Saito, A. Iwabuchi, and T. Shimizu, "Effects of Co content and WC grain size on wear of WC cemented carbide," *Wear*, vol. 261, no. 2, pp. 126–132, Jul. 2006.

[33] K. Jia, T. E. Fischer, and B. Gallois, "Microstructure, hardness and toughness of nanostructured and conventional WC-Co composites," *Nanostructured Mater.*, vol. 10, no. 5, pp. 875–891, Jul. 1998.

[34] A. Love, S. Luyckx, and N. Sacks, "Quantitative relationships between magnetic properties, microstructure and composition of WC-Co alloys," *J. Alloys Compd.*, vol. 489, no. 2, pp. 465–468, Jan. 2010.

[35] R. T. Faria, M. F. Rodrigues, I. De Andrade Esquef, H. Vargas, and M. Filgueira, "On the thermal characterization of a HPHT sintered WC-15% wt Co hardmetal alloy," *Int. J. Refract. Met. Hard Mater.*, vol. 23, no. 2, pp. 115–118, Mar. 2005.

[36] H. Wang, T. Webb, and J. W. Bitler, "Study of thermal expansion and thermal conductivity of cemented WC-Co composite," *Int. J. Refract. Met. Hard Mater.*, vol. 49, no. 1, pp. 170–177, 2015.

[37] T. Kagnaya, C. Boher, L. Lambert, M. Lazard, and T. Cutard, "Wear mechanisms of WC–Co cutting tools from high-speed tribological tests," *Wear*, vol. 267, 2009.

[38] B. Darvell, *Materials science for dentistry*. 2009.